

# *Swift*/XRT monitoring of the Supergiant Fast X-ray Transient IGR J18483–0311 for an entire orbital period

P. Romano<sup>1</sup>, L. Sidoli<sup>2</sup>, L. Ducci<sup>3,2</sup>, G. Cusumano<sup>1</sup>, V. La Parola<sup>1</sup>, C. Pagani<sup>4</sup>, K.L. Page<sup>5</sup>, J.A. Kennea<sup>4</sup>, D.N. Burrows<sup>4</sup>, N. Gehrels<sup>6</sup>, V. Sguera<sup>7</sup>, A. Bazzano<sup>7</sup>

<sup>1</sup>INAF, Istituto di Astrofisica Spaziale e Fisica Cosmica, Via U. La Malfa 153, I-90146 Palermo, Italy

<sup>2</sup>INAF, Istituto di Astrofisica Spaziale e Fisica Cosmica, Via E. Bassini 15, I-20133 Milano, Italy

<sup>3</sup>Dipartimento di Fisica e Matematica, Università dell'Insubria, Via Valleggio 11, I-22100 Como, Italy

<sup>4</sup>Department of Astronomy and Astrophysics, Pennsylvania State University, University Park, PA 16802, USA

<sup>5</sup>Department of Physics & Astronomy, University of Leicester, LE1 7RH, UK

<sup>6</sup>NASA/Goddard Space Flight Center, Greenbelt, MD 20771, USA

<sup>7</sup>INAF, Istituto di Astrofisica Spaziale e Fisica Cosmica, Via Fosso del Cavaliere 100, I-00133, Roma, Italy

Accepted 2009 September 25. Received 2009 September 23; in original form 2009 July 23

## ABSTRACT

IGR J18483–0311 is an X-ray pulsar with transient X-ray activity, belonging to the new class of High Mass X-ray Binaries called Supergiant Fast X-ray Transients. This system is one of the two members of this class, together with IGR J11215–5952, where both the orbital (18.52 d) and spin period (21 s) are known. We report on the first complete monitoring of the X-ray activity along an entire orbital period of a Supergiant Fast X-ray Transient. These *Swift* observations, lasting 28 days, cover more than one entire orbital phase consecutively. They are a unique data-set, which allows us to constrain the different mechanisms proposed to explain the nature of this new class of X-ray transients. We applied the new clumpy wind model for blue supergiants developed by Ducci et al. (2009), to the observed X-ray light curve. Assuming an eccentricity of  $e = 0.4$ , the X-ray emission from this source can be explained in terms of the accretion from a spherically symmetric clumpy wind, composed of clumps with different masses, ranging from  $10^{18}$  g to  $5 \times 10^{21}$  g.

**Key words:** X-rays: binaries - X-rays: individual (IGR J18483–0311)

## 1 INTRODUCTION

The X-ray transient IGR J18483–0311 was discovered during the observations of the Galactic plane with *INTEGRAL* in April 2003 (Chernyakova et al. 2003), when it reached a flux of 10 mCrab in the 15–40 keV energy range. Five more hard X-ray outbursts were reported by Sguera et al. (2007) with *INTEGRAL*, three of which exceeded one day in duration. The strongest outburst ( $\sim 1.8$  days) occurred in April 2006 and reached a flux of 120 mCrab. The IGR J18483–0311 broad band joint JEM-X/ISGRI *INTEGRAL* spectrum (3–50 keV) was fitted with an absorbed power law with a photon index,  $\Gamma = 1.4 \pm 0.3$ , a high absorption,  $N_H = 9_{-4}^{+5} \times 10^{22} \text{ cm}^{-2}$  (higher than the Galactic at  $1.4 \times 10^{22} \text{ cm}^{-2}$ ), and a cutoff at  $\sim 22$  keV (Sguera et al. 2007).

A periodicity at  $18.55 \pm 0.03$  days was discovered in the ASM/RXTE light curves (Levine & Corbet 2006), and was interpreted as the orbital period of a binary system. Sguera et al. (2007) confirmed a similar period in the 20–40 keV ISGRI/*INTEGRAL* data ( $18.52 \pm 0.01$  days) and discovered pulsations at  $21.0526 \pm 0.0005$  s with the X-ray monitor JEM-X. Skinner et al. (2008) re-

finned the orbital period value to  $18.518 \pm 0.005$  d, by using the much denser sampling provided by the *Swift*/BAT data.

From the observed values of the orbital and pulse periods, the position in the Corbet diagram (Corbet 1986) suggested at first a Be/X-ray transient nature (Sguera et al. 2007), but the optical and infrared observations of the X-ray error box estimated with *Swift* (Sguera et al. 2007) revealed that the donor star is a blue supergiant (B0.5Ia), and not a Be star, located at a distance of 3–4 kpc (Rahoui & Chaty 2008). The X-ray position was later refined with *Chandra* (Giunta et al. 2009), confirming this optical/IR association. This implied the identification of this source as a new member of the class of the Supergiant Fast X-ray Transients (SFXTs; Sguera et al. 2005, Sguera et al. 2006, Negueruela et al. 2006, Sidoli 2009), although the dynamical range of its X-ray emission seems to be smaller than in other members of the same class. IGR J18483–0311 and IGR J11215–5952 are the only two SFXTs where both orbital and pulse periods have been discovered (Swank et al. 2007, Sidoli et al. 2006, Romano et al. 2009b).

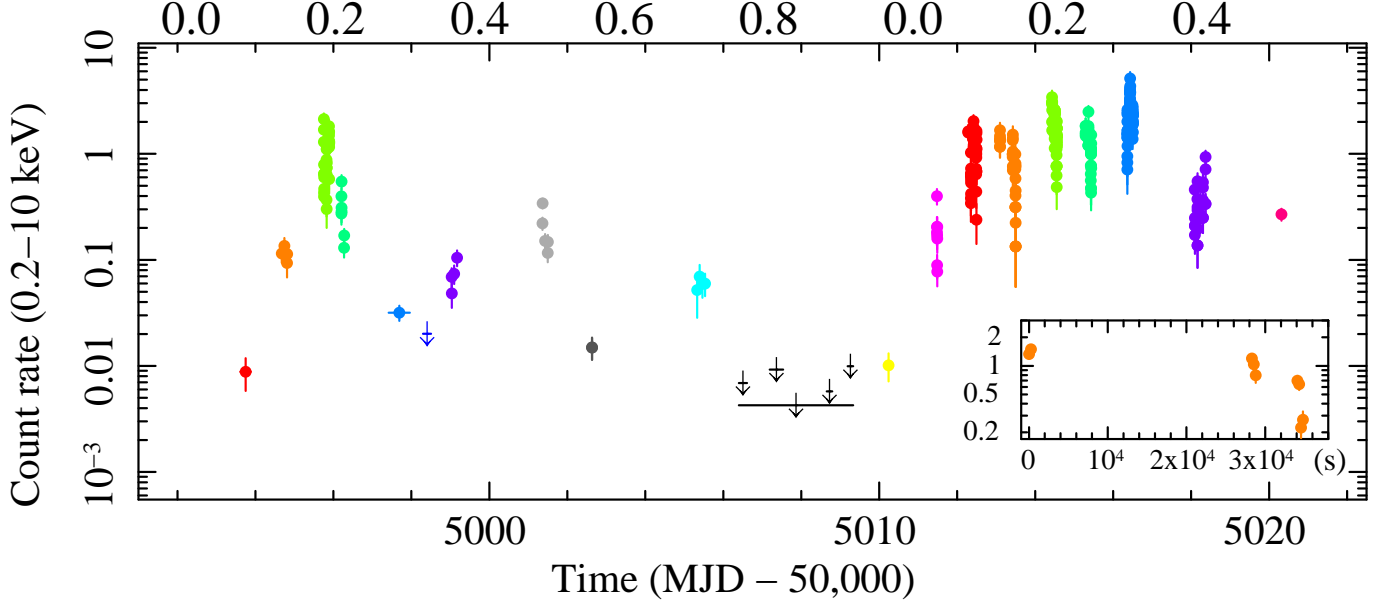


**Figure 1.** *Swift*/XRT 0.2–10 keV light curve of IGR J18483–0311 during our monitoring program, background-subtracted and corrected for pile-up, PSF losses, and vignetting. Downward-pointing arrows are  $3\sigma$  upper limits. The upper limit with the wide symbol centered on MJD 55007.9 ( $\sim 0.004$  counts  $\text{s}^{-1}$ ) is obtained accumulating the 4 observations (individual upper limits) between MJD 55006.5 and 55010.2. Different colours mark different observations (see Table 1), with a colour scheme that generally mimics the phase (top axis) with a  $P = 18.52$  days (Sguera et al. 2007). The inset zooms on observation 024.

**Table 1.** Summary of the *Swift*/XRT observations.

Seq.	Start time (UT)	End time (UT)	Exp. (s)	Phase <sup>a</sup>
004	2009-06-11 14:42:17	2009-06-11 21:13:56	1606	0.07
005	2009-06-12 16:09:36	2009-06-12 19:34:56	1522	0.12
006	2009-06-13 18:08:11	2009-06-13 21:26:57	1774	0.18
007	2009-06-14 04:55:39	2009-06-14 08:20:57	1671	0.21
008	2009-06-15 10:03:12	2009-06-15 23:02:58	1977	0.28
009	2009-06-16 07:10:02	2009-06-16 12:08:58	1857	0.32
010	2009-06-17 00:42:44	2009-06-17 04:12:56	2047	0.36
012	2009-06-19 08:37:38	2009-06-19 12:02:56	2189	0.49
013	2009-06-20 13:32:09	2009-06-20 16:57:56	2291	0.55
016	2009-06-23 07:51:16	2009-06-23 12:53:56	2003	0.70
017	2009-06-24 09:32:31	2009-06-24 14:35:56	2711	0.76
018	2009-06-25 04:33:46	2009-06-25 12:52:56	1870	0.81
019	2009-06-26 15:43:27	2009-06-26 19:06:57	1884	0.88
020	2009-06-27 04:33:51	2009-06-27 07:56:57	1824	0.91
021	2009-06-28 03:16:17	2009-06-28 08:14:56	1922	0.96
022	2009-06-29 11:30:17	2009-06-29 11:47:57	1057	0.03
023	2009-06-30 06:47:17	2009-06-30 11:54:57	2616	0.08
024	2009-07-01 02:17:22	2009-07-01 12:00:57	2070	0.13
025	2009-07-02 10:22:32	2009-07-02 13:23:57	2408	0.19
026	2009-07-03 07:01:47	2009-07-03 10:31:58	2106	0.24
027	2009-07-04 07:05:17	2009-07-04 10:36:27	2560	0.29
029	2009-07-06 02:15:18	2009-07-06 08:53:58	1838	0.39
030	2009-07-08 07:32:02	2009-07-08 07:37:56	340	0.51

<sup>a</sup> Calculated according to Sguera et al. (2007).

## 2 OBSERVATIONS AND DATA REDUCTION

The observations of IGR J18483–0311 were obtained as a Target of Opportunity (ToO) monitoring program with *Swift*. As shown in

Table 1, the ToO observations started on 2009 June 11 with  $\sim 2$  ks per day. The campaign lasted 28 days divided in 23 observations for a total on-source exposure of  $\sim 44$  ks.

The XRT data were processed with standard procedures (XRTPIPELINE v0.12.1), filtering and screening criteria by using FTOOLS in the HEASOFT package (v6.6.1). Both WT and PC events were considered. The selection of event grades was 0–2 and 0–12, for WT and PC data, respectively (Burrows et al. 2005). We corrected for pile-up when required. The light curves were also corrected for PSF losses, vignetting and background-subtracted. Ancillary response files were generated with XRTMKARF, to account for different extraction regions, vignetting, and PSF corrections. We used the spectral redistribution matrices v011 in CALDB.

The UVOT observed the target simultaneously with the XRT with the  $v$  filter (observations 004 through 006), and with the  $u$  filter (observations 007 through 010). For the remainder of the campaign IGR J18483–0311 was observed with the ‘Filter of the Day’, i.e. the filter chosen for all observations to be carried out during a specific day in order to minimize the filter wheel usage (Roming et al. 2005). The data analysis was performed using the UVOTISUM and UVOTSOURCE tasks included in the FTOOLS. The latter task calculates the magnitude through aperture photometry within a circular region and applies specific corrections due to the detector characteristics. The reported magnitudes are on the UVOT photometric system described in Poole et al. (2008), and are not corrected for Galactic extinction. At the position of IGR J18483–0311, no detection was achieved down to a limit of  $v > 21.07$  mag and  $u > 21.19$  mag.

All quoted uncertainties are given at 90 % confidence level for one interesting parameter unless otherwise stated. The spectral indices are parameterized as  $F_\nu \propto \nu^{-\alpha}$ , where  $F_\nu$  (erg  $\text{cm}^{-2} \text{s}^{-1} \text{Hz}^{-1}$ ) is the flux density as a function of frequency  $\nu$ ; we adopt  $\Gamma = \alpha + 1$  as the photon index,  $N(E) \propto E^{-\Gamma}$  (ph  $\text{cm}^{-2} \text{s}^{-1} \text{keV}^{-1}$ ).

**Table 2.** XRT spectroscopy.

Seq.	Power-law $N_H$ ( $10^{22}$ cm $^{-2}$ )	$\Gamma$	Flux <sup>a</sup> (2–10 keV)	$\chi^2_{\text{red}}/\text{dof}$ C-stat (%) <sup>c</sup>	Black body $N_H$ ( $10^{22}$ cm $^{-2}$ )	$kT$ (keV)	$R_{\text{BB}}$ (km) <sup>d</sup>	Flux <sup>a</sup> (2–10 keV)	$L^b$ (2–10 keV)	$\chi^2_{\text{red}}/\text{dof}$ C-stat (%) <sup>c</sup>
005	$6.0^{+3.4}_{-2.5}$	$1.4^{+0.9}_{-0.8}$	$1.90^{+0.37}_{-0.94}$	102.1(48.3)	$3.5^{+2.2}_{-1.6}$	$1.6^{+0.6}_{-0.4}$	$0.14^{+0.03}_{-0.01}$	$1.46^{+0.15}_{-0.83}$	0.2	100.9(31.90)
006	$6.3^{+1.5}_{-1.2}$	$1.7^{+0.4}_{-0.4}$	$15.46^{+0.54}_{-3.45}$	1.1/34	$3.1^{+0.8}_{-0.7}$	$1.6^{+0.2}_{-0.2}$	$0.43^{+0.22}_{-0.14}$	$11.3^{+0.79}_{-1.99}$	1.2	1.1/34
007	$4.8^{+3.8}_{-2.1}$	$1.3^{+0.9}_{-0.7}$	$2.72^{+0.39}_{-0.92}$	1.2/9	$2.5^{+2.0}_{-1.2}$	$1.6^{+0.5}_{-0.3}$	$0.17^{+0.04}_{-0.02}$	$2.06^{+0.24}_{-0.99}$	0.2	0.9/9
010	$6.6^{+2.7}_{-2.2}$	$2.1^{+0.8}_{-0.7}$	$1.45^{+0.12}_{-0.68}$	119.0(27.2)	$3.5^{+1.7}_{-1.4}$	$1.3^{+0.3}_{-0.2}$	$0.18^{+0.05}_{-0.02}$	$1.00^{+0.10}_{-0.46}$	0.1	117.5(10.58)
012	$6.4^{+3.0}_{-2.1}$	$1.8^{+0.7}_{-0.6}$	$2.78^{+0.19}_{-1.05}$	1.2/13	$3.2^{+1.7}_{-1.2}$	$1.5^{+0.3}_{-0.2}$	$0.20^{+0.05}_{-0.02}$	$1.98^{+0.16}_{-0.71}$	0.2	1.1/13
022	$16.5^{+7.7}_{-6.1}$	$2.3^{+1.2}_{-1.1}$	$5.79^{+0.30}_{-4.33}$	97.43(26.7)	$10.7^{+5.2}_{-4.0}$	$1.5^{+0.6}_{-0.3}$	$0.27^{+0.28}_{-0.08}$	$3.43^{+0.22}_{-2.24}$	0.4	98.02(12.17)
023	$6.6^{+1.4}_{-1.2}$	$1.4^{+0.3}_{-0.3}$	$17.44^{+0.51}_{-3.38}$	0.9/51	$3.7^{+0.8}_{-0.7}$	$1.7^{+0.2}_{-0.2}$	$0.39^{+0.15}_{-0.10}$	$13.26^{+0.62}_{-2.14}$	1.4	1.0/51
024	$10.4^{+2.9}_{-2.3}$	$1.5^{+0.5}_{-0.4}$	$19.97^{+0.58}_{-6.79}$	0.7/25	$6.3^{+1.8}_{-1.4}$	$1.9^{+0.3}_{-0.3}$	$0.37^{+0.19}_{-0.11}$	$14.78^{+0.84}_{-4.13}$	1.6	0.7/25
025	$7.1^{+1.1}_{-1.0}$	$1.6^{+0.3}_{-0.3}$	$32.83^{+0.87}_{-4.92}$	1.1/71	$3.8^{+0.7}_{-0.6}$	$1.7^{+0.2}_{-0.1}$	$0.56^{+0.38}_{-0.27}$	$24.23^{+0.92}_{-3.19}$	2.6	1.2/71
026	$6.3^{+1.3}_{-1.1}$	$1.2^{+0.3}_{-0.3}$	$20.83^{+0.88}_{-3.87}$	1.0/42	$3.7^{+0.8}_{-0.7}$	$1.9^{+0.2}_{-0.2}$	$0.38^{+0.14}_{-0.09}$	$16.68^{+0.94}_{-3.08}$	1.8	1.0/42
027	$6.6^{+0.9}_{-0.8}$	$1.3^{+0.2}_{-0.2}$	$43.22^{+1.18}_{-5.46}$	0.8/81	$3.8^{+0.6}_{-0.5}$	$1.9^{+0.2}_{-0.1}$	$0.56^{+0.29}_{-0.22}$	$34.14^{+1.39}_{-3.64}$	3.7	0.8/81
029	$7.9^{+2.6}_{-1.9}$	$1.8^{+0.5}_{-0.5}$	$6.55^{+0.20}_{-2.17}$	1.4/25	$4.3^{+1.4}_{-1.1}$	$1.6^{+0.2}_{-0.2}$	$0.28^{+0.09}_{-0.05}$	$4.64^{+0.30}_{-1.18}$	0.5	1.3/25
high <sup>e</sup>	$5.4^{+0.5}_{-0.4}$	$1.0^{+0.1}_{-0.1}$	$25.77^{+0.46}_{-1.48}$	1.0/222	$3.2^{+0.3}_{-0.3}$	$2.1^{+0.1}_{-0.1}$	$0.37^{+0.05}_{-0.04}$	$21.25^{+0.56}_{-1.21}$	2.3	1.2/222
medium <sup>e</sup>	$6.4^{+0.6}_{-0.5}$	$1.2^{+0.1}_{-0.1}$	$16.47^{+0.28}_{-1.06}$	1.0/212	$3.7^{+0.4}_{-0.3}$	$2.0^{+0.1}_{-0.1}$	$0.32^{+0.03}_{-0.03}$	$13.14^{+0.33}_{-0.69}$	1.4	1.1/212
low <sup>e</sup>	$6.7^{+0.9}_{-0.8}$	$1.5^{+0.2}_{-0.2}$	$1.82^{+0.16}_{-0.06}$	1.0/115	$3.6^{+0.5}_{-0.5}$	$1.7^{+0.1}_{-0.1}$	$0.130^{+0.003}_{-0.002}$	$1.38^{+0.04}_{-0.11}$	0.2	0.8/115

<sup>a</sup> Fluxes (corrected for the absorption) are in units of  $10^{-11}$  erg cm $^{-2}$  s $^{-1}$ .

<sup>b</sup> Luminosities in units of  $10^{35}$  erg s $^{-1}$ , assuming a distance of 3 kpc.

<sup>c</sup> Cash statistics (C-stat) and percentage of  $10^4$  Monte Carlo realizations that had statistics < C-stat.

<sup>d</sup> Blackbody radii are in units of km, assuming the optical counterpart distance of 3 kpc.

<sup>e</sup> Intensity-selected spectra. High corresponds to  $CR > 1$  counts s $^{-1}$ , medium to  $0.5 < CR < 1$  counts s $^{-1}$ , and low to  $CR < 0.5$  counts s $^{-1}$ .

### 3 RESULTS

#### 3.1 Light curve

Fig. 1 shows the 0.2–10 keV light curve of IGR J18483–0311 of the whole campaign after background-subtraction and pile-up, PSF losses, and vignetting corrections. Each bin contains a minimum of 20 source counts. The light curve starts at phase 0.07, assuming a period of 18.52 d and an initial epoch MJD 53844.2 (Sguera et al. 2007), and monitors the flux state through a whole period until the following phase 0.51. Superimposed on the long-term orbital modulation, variability is seen on short time scales, as shown in the inset of Fig. 1, where a variation by factor of 5.3 in count rate is observed to occur in  $\sim 1.7$  hr. This behaviour has been observed in several SXTs (e.g., Sidoli et al. 2008; Romano et al. 2009a).

The lowest point in the campaign is a  $3\sigma$  upper limit reached on MJD 55006.5–55010.2 at 0.004 counts s $^{-1}$  (combined observations 017–020, total on-source exposure of 8.3 ks), and corresponds to an observed (unabsorbed) flux of  $3.9 \times 10^{-13}$  ( $2.1 \times 10^{-12}$ ) erg cm $^{-2}$  s $^{-1}$ , if we assume the *XMM-Newton* spectrum reported by Giunta et al. (2009, photon index  $\Gamma = 2.5$ , absorbing column  $N_H = 7.7 \times 10^{22}$  cm $^{-2}$ ). The corresponding luminosity is  $2.3 \times 10^{33}$  erg s $^{-1}$  (assuming the optical counterpart distance of 3 kpc); to date this is the lowest quiescent X-ray flux value reported in the literature for this source. The peak count rate is reached on MJD 55016.4 at  $\gtrsim 5$  counts s $^{-1}$ ; therefore, the observed dynamical range of this source is at least 1200.

In order to search for spin periodicity, the arrival times of all selected events have been converted to the Solar System barycentric frame, using the BARYCOR code. The  $Z^2$  test (Buccheri et al. 1983) on the fundamental harmonics was applied to a sample of source photon arrival times for each observation. The search for a timing

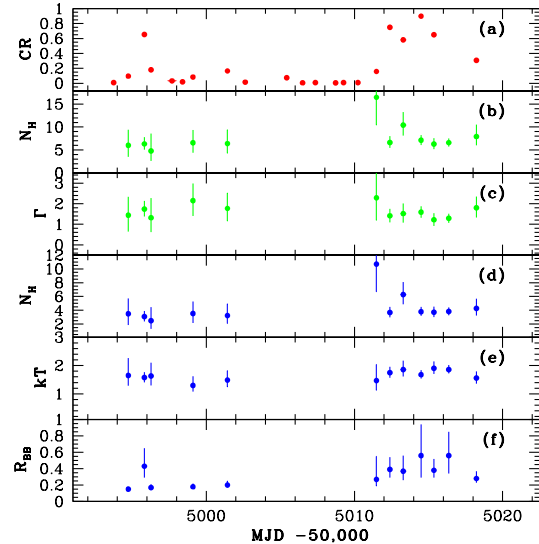


**Figure 2.** Spectral parameters as a function of time (see Table 2). (a) *Swift*/XRT light curve in the 0.2–10 keV energy band at a day resolution; Spectral parameters of the absorbed power-law fit,  $N_H$ , and photon index  $\Gamma$  [(b) and (c)]; Spectral parameters of the absorbed blackbody fit,  $N_H$ , temperature  $kT$ , and blackbody radius [(d), (e), and (f)].

feature was performed within the frequency interval 0.01–0.19 s $^{-1}$ . No presence of coherent pulsations was detected.

### 3.2 Spectra

Spectra were extracted for each segment in which a detection was obtained and a minimum of 120 source counts were available. The data were rebinned with at least 20 counts  $\text{bin}^{-1}$  to allow  $\chi^2$  fitting, except when the statistics were poor, in which case we adopted Cash (1979) statistics and data binned to 1 count  $\text{bin}^{-1}$ , instead. The simple models we considered were absorbed power laws and absorbed blackbodies. The fits were performed in the 0.3–10 keV energy band. The results are reported in Table 2, while the spectral parameters as a function of time are shown in Fig. 2. In particular, for the spectrum of observation 006, the highest in flux during the first peak ( $\sim 1.5 \times 10^{-10} \text{ erg cm}^{-2} \text{ s}^{-1}$ ), an absorbed power-law model yielded a high absorbing column  $N_{\text{H}} = (6.3^{+1.5}_{-1.2}) \times 10^{22} \text{ cm}^{-2}$ , and a photon index  $\Gamma = 1.7 \pm 0.4$  (see Table 2). As a comparison, observation 025, roughly at the same phase, yielded  $N_{\text{H}} = (7.1^{+1.1}_{-1.0}) \times 10^{22} \text{ cm}^{-2}$ , and  $\Gamma = 1.6 \pm 0.3$ , hence consistent with observation 006. Despite the large observed variations in flux throughout the campaign, the spectral parameters do not vary significantly within the large uncertainties, with the exception of the blackbody radii.

To further investigate the spectral properties of the sources in several states, we accumulated all events collected during the current campaign. We extracted events within three intensity levels depending on count rate, namely,  $CR > 1 \text{ counts s}^{-1}$  (high, 5447 counts),  $0.5 < CR < 1 \text{ counts s}^{-1}$  (medium, 5264 counts), and  $CR < 0.5 \text{ counts s}^{-1}$  (low, 2670 counts). We created exposure maps for each of these intensity-selected event files and then combined them (and their exposure maps), and extracted a single spectrum for state. The generation of ancillary response files and spectral fitting were performed in the same fashion as for the single observations. The fit results are reported in Table 2 and the spectra are shown in Fig. 3. Even with the higher statistics afforded by accumulating all events in three intensity states, no significant variations in the column density could be derived. We can confirm, however, that the  $N_{\text{H}}$  is always in excess of the Galactic one,  $1.4 \times 10^{22} \text{ cm}^{-2}$ , consistently with that found by Sguera et al. (2007). Similarly to what was found in a sample of 4 SFXTs (Romano et al. 2009a), our fits indicate either a hard power law or hot black body. We also note that all spectral fits with an absorbed black body resulted in radii of the emitting black body region of only a few hundred meters (see Table 2), consistent with being emitted from a small portion of the neutron star surface, such as its polar caps (see, Romano et al. 2009a).

## 4 DISCUSSION

In this paper we report on the first complete monitoring of the X-ray activity along an entire orbital period of a Supergiant Fast X-ray Transient. This makes these *Swift* observations a unique dataset, which allows us to constrain the different mechanisms proposed to explain the nature of this new class of X-ray transients. IGR J18483–0311 and IGR J11215–5952 are the only SFXTs where both the orbital and spin periods are known, although the two systems are very different ( $P_{\text{orb}} \sim 165 \text{ days}$ ,  $P_{\text{spin}} \sim 190 \text{ s}$ , in IGR J11215–5952; see, e.g., Romano et al. 2009b).

The *Swift* light curve appears to be highly modulated, with two maxima, separated by a time interval consistent with the orbital period of  $\sim 18.5 \text{ days}$ . A lower limit of 1200 to the dynamical range can be obtained from the observed light curve. The different duration of the two outburst peaks monitored with *Swift* is probably

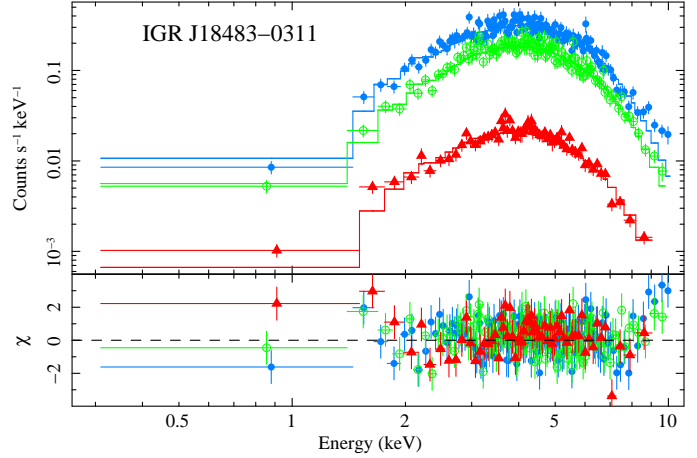


**Figure 3.** Intensity-selected spectroscopy. Upper panel: *Swift*/XRT data fit with an absorbed power law. Lower panel: the residuals of the fit (in units of standard deviations). Filled blue circles, green empty circles, and red filled triangles mark high, medium, and low state, respectively.

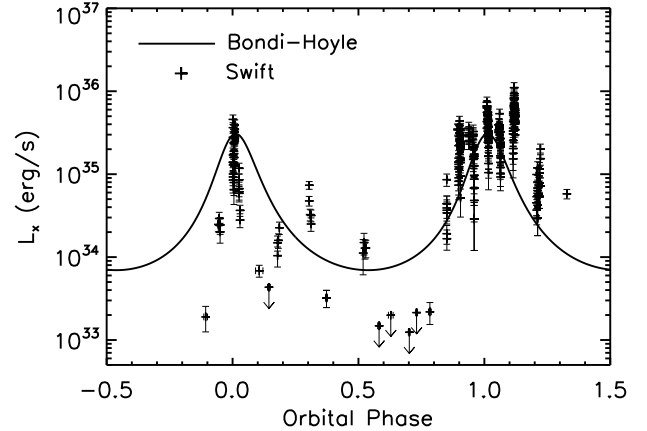


**Figure 4.** Comparison of the *Swift*/XRT light curve of IGR J18483–0311 (crosses) with the prediction of Bondi-Hoyle accretion from a spherically symmetric and homogeneous wind. We assumed a distance of 3 kpc. The model-dependent orbital phase  $\phi = 0$  corresponds to 54995.83 MJD.

the result of both a different sampling and a high intrinsic X-ray variability. The second peak has a duration of several days, as previously observed by INTEGRAL (Sguera et al. 2007).

The modulation of the overall shape of the light curve with the orbital phase can be interpreted as wind accretion along a highly eccentric orbit. Thus, we applied different models for the wind accretion to gain information on the source parameters.

The simplest case is a Bondi-Hoyle accretion from a spherically symmetric and homogeneous wind. Assuming a supergiant mass of  $M_{\text{OB}} = 33 M_{\odot}$  and a radius,  $R_{\text{OB}} = 33.8 R_{\odot}$  (Searle et al. 2008), together with the known orbital period of  $P_{\text{orb}} = 18.52 \text{ d}$ , we tried to account for the overall shape of the X-ray light curve, leaving the orbital eccentricity  $e$  as a free parameter. We assumed the following values for the wind properties: a terminal velocity  $v_{\infty}$  in the range 1400–1800  $\text{km s}^{-1}$ , a mass loss rate  $\dot{M}$  in the range  $0.4\text{--}1.5 \times 10^{-6} M_{\odot} \text{ yr}^{-1}$  [see Searle et al. (2008), Lefever et al. (2007)]. In this framework, we obtain the best agreement with the observed light curve by assuming an eccentric-

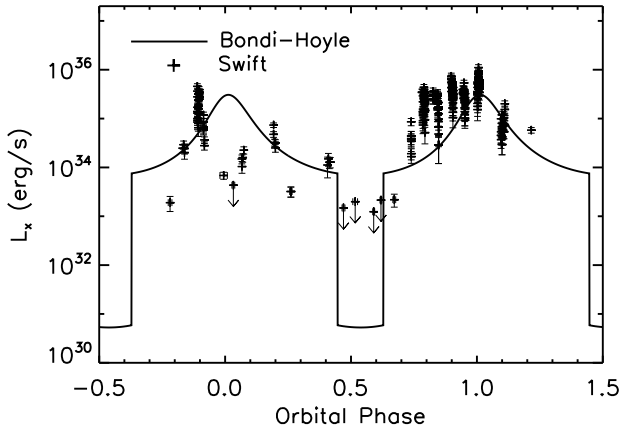


**Figure 5.** Comparison of the *Swift*/XRT light curve of IGR J18483–0311 (crosses) with the prediction of Bondi-Hoyle accretion from a spherically symmetric and homogeneous wind, assuming a magnetic field  $B = 4 \times 10^{11}$  G. The model-dependent orbital phase  $\phi = 0$  corresponds to 54997.69 MJD.

ity  $e = 0.4$ ,  $v_\infty = 1800 \text{ km s}^{-1}$ ,  $\dot{M} = 5 \times 10^{-7} \text{ M}_\odot \text{ yr}^{-1}$ ,  $\beta = 1$ . Fig. 4 shows the comparison of the model predictions and the observed *Swift*/XRT light curve (in units of  $\text{ergs s}^{-1}$ , by assuming a distance of 3 kpc). The model roughly reproduces the shape of the X-ray light curve due to the orbital modulation, with the largest deviation from the observations being in the time interval MJD 55006.5–55010.2, where we observed 4 upper limits. Note, however, that we cannot be sure that the low intensity extends for 4 days continuously, because the four *Swift* observations consist of short snapshots. We investigated the possibility that these upper limits could be due to the onset of a centrifugal inhibition for the accretion (Davidson & Ostriker 1973). For the above adopted set of wind and orbital parameters, we calculated a new X-ray light curve, finding that a low magnetic field of the neutron star of  $B \approx 4 \times 10^{11}$  G could be responsible for the upper limits at MJD 55006.5–55010.2 (see Fig. 5).

An alternative scenario to explain the low intensity state is an X-ray eclipse of the neutron star by the supergiant companion. Assuming a circular orbit, we obtain a lower limit to the radius of the supergiant star (Rappaport & Joss 1983) of  $R_{\text{OB}} = 46 R_\odot$ , which is too large for a B0.5a supergiant (Searle et al. 2008). On the other hand, our modelling of the X-ray curve suggests a high eccentricity of at least  $e = 0.4$ . Adopting this eccentricity, we derived an expected value for the supergiant radius of  $R_{\text{OB}} = 39.5 R_\odot$ . The radii of B0.5Ia stars are usually smaller than this value, but there are several exceptions with  $R \approx 40 R_\odot$  (Searle et al. 2008; Lefever et al. 2007). Therefore we cannot exclude that an eclipse is responsible for the low luminosity state, in an eccentric orbit.

Although both centrifugal inhibition and an eclipse can reconcile the observed low intensity state with the Bondi-Hoyle accretion predictions, it is also clear that the spherically symmetric and homogeneous wind only reproduces the overall shape of the X-ray light curve. It cannot, indeed, account for the very large spread around the average behaviour due to the orbital modulation and, most of all, the remarkable short time scale variability (see, for example, the inset in Fig. 1, where a variation by a factor of 5.3 in count rate is observed in  $\sim 1.7$  hours). The observed short time scale variability can be naturally explained by the accretion of single clumps composing the donor wind. Thus, in order to im-

prove the agreement between the observed and the calculated light curve, we applied the isotropic clumpy wind model proposed by Ducci et al. (2009).

The Ducci et al. (2009) model was developed to investigate the effects of accretion from a clumpy wind on the luminosity and variability properties of HMXBs. It assumes that a fraction of the stellar wind is in the form of clumps with a power law mass distribution

$$p(M_{\text{cl}}) = k \left( \frac{M_{\text{cl}}}{M_a} \right)^{-\zeta} \quad (1)$$

in the mass range  $M_a$ – $M_b$ . The rate of clumps produced by the supergiant is related to the total mass loss rate  $\dot{M}_{\text{tot}}$  by  $N_{\text{cl}} = \frac{f \dot{M}_{\text{tot}}}{\langle M \rangle}$  clumps  $\text{s}^{-1}$ , where  $f = \dot{M}_{\text{cl}} / \dot{M}_{\text{tot}}$  is the fraction of mass lost in clumps and  $\langle M \rangle$  is the average clump mass, which can be computed from Eq. (1). Clumps are driven radially outward by absorption of UV spectral lines. The following clump velocity profile is assumed:  $v_{\text{cl}}(r) = v_\infty \left( 1 - 0.9983 \frac{R_{\text{OB}}}{r} \right)^\beta$ , where  $v_\infty$  is the terminal wind velocity,  $R_{\text{OB}}$  is the radius of the supergiant, 0.9983 is a parameter which ensures that  $v(R_{\text{OB}}) \approx 10 \text{ km s}^{-1}$ , and  $\beta$  is a constant in the range  $\sim 0.5$ – $1.5$ . The model further assumes that the clumps are confined by ram pressure of the ambient gas. By exploring different distributions for the clump masses and initial dimensions, the model can be used to compute the expected X-ray light curves in the framework of the Bondi-Hoyle accretion theory, modified to take into account the presence of clumps. We sought the set of wind parameters yielding the best agreement between the calculated and the observed light curve. We found that the observed light curve is reproduced well by this wind model by assuming the following parameter values: an eccentricity  $e = 0.4$ , a mass loss rate  $\dot{M}_{\text{tot}} = 2 \times 10^{-7} \text{ M}_\odot \text{ yr}^{-1}$ ,  $v_\infty = 1800 \text{ km s}^{-1}$ ,  $\beta = 1$ , a fraction of mass lost in clumps  $f = 0.75$ , a mass distribution power law index  $\zeta = 1.1$ , a power law index of the initial clump dimension distribution  $\gamma = -1$  (where  $\dot{N}_{\text{cl}} \propto R_{\text{cl}}^\gamma$  clumps  $\text{s}^{-1}$ ), a minimum clump mass  $M_a = 10^{18} \text{ g}$  and a maximum clump mass  $M_b = 5 \times 10^{21} \text{ g}$ ; moreover, we adopt the force multiplier parameter obtained by Shimada et al. (1994) for a B0.5Ia star ( $k = 0.375$ ,  $\alpha = 0.522$ ,  $\delta = 0.099$ ).

Fig. 6 shows the comparison of the *Swift*/XRT light curve of IGR J18483–0311 with the isotropic clumpy wind model prediction. Further acceptable solutions can be found by assuming wind parameters  $\zeta$ ,  $f$ ,  $\gamma$  in the allowed ranges plotted in Fig. 7, and  $e = 0.4 \pm 0.1$ ,  $\dot{M}_{\text{tot}} = (2 \pm 1) \times 10^{-7} \text{ M}_\odot \text{ yr}^{-1}$ ,  $v_\infty = 1800 \text{ km s}^{-1}$ ,  $\beta = 1$ ,  $10^{18} \leq M_{\text{cl}} \leq 10^{21} \text{ g}$ . As Fig. 7 demonstrates, the comparison of the observed light curve with the clumpy wind model allowed us to constrain the parameters responsible for the degree of inhomogeneity of the wind. In particular, we found that a very large fraction of the mass lost from the supergiant is contained in the clumps ( $0.7 \lesssim f \lesssim 0.78$ ), and we obtain the value of  $\zeta$  (which controls the shape of the clump formation rate distribution) with an accuracy of  $\sim 15\%$ .

Fig. 6 shows that the peak luminosities, the dynamic range involved by the flares, and the orbital modulation and the low luminosity state (MJD 55006.5–55010.2) observed are reproduced well by the clumpy wind model, even without invoking either a centrifugal barrier or an X-ray eclipse. Indeed, from the calculated light curve, we determined that the probability to observe the source at the inter-clump luminosity level in the range of phase  $0.2 < \phi < 0.8$  is  $\sim 25\%$ : with the binomial distribution function, we obtain a probability to measure 4 low luminosity states of  $\sim 5\%$ . Therefore, the upper limits can be explained with the accretion of the intra-clump wind with a low density, even with-

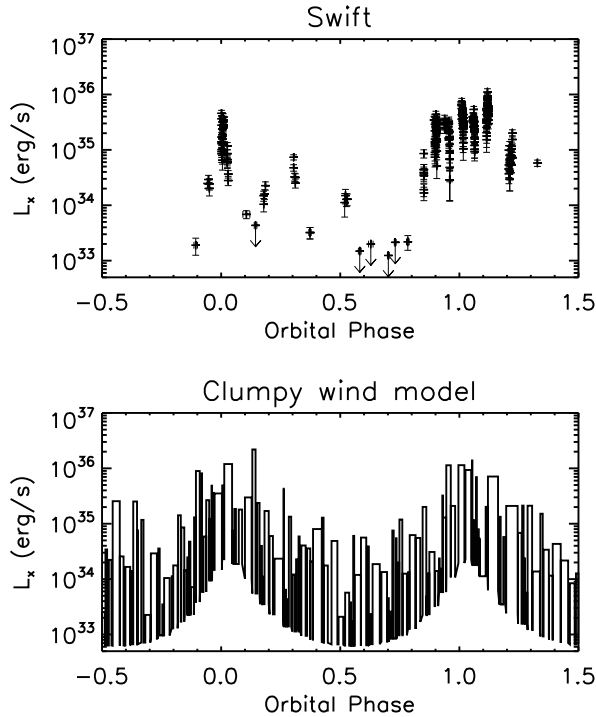


**Figure 6.** Comparison of the *Swift*/XRT light curve of IGR J18483–0311 (top) with the prediction (bottom) of the new clumpy wind model of Ducci et al. (2009). The model-dependent orbital phase  $\phi = 0$  corresponds to 54995.83 MJD.

out invoking centrifugal inhibition or an eclipse. Finally, we note that the wind parameters we obtain applying our spherical clumpy wind model (Ducci et al. 2009) are very similar to those explaining the Vela X–1 X-ray light curve. Indeed, the two systems have very similar donor stars.

## ACKNOWLEDGMENTS

We thank the *Swift* team duty scientists and science planners. We also thank the remainder of the *Swift* XRT and BAT teams, S. Barthelmy and J.A. Nousek, in particular, for their invaluable help and support. This work was supported in Italy by contracts ASI I/088/06/0 and I/023/05/0, at PSU by NASA contract NAS5-00136. We thank P.A. Evans and S. Vercellone for helpful discussions. We also thank the anonymous referee for comments that helped improve the paper.

## REFERENCES

- Buccheri, R., Bennett, K., Bignami, G. F., et al. 1983, *A&A*, 128, 245  
 Burrows, D. N., Hill, J. E., & Nousek, J. A., et al., 2005, *Space Science Reviews*, 120, 165  
 Cash, W. 1979, *ApJ*, 228, 939  
 Chernyakova, M., Lutovinov, A., Capitanio, F., Lund, N., & Gehrels, N. 2003, *Astron. Tel.*, 157  
 Corbet, R. H. D. 1986, *MNRAS*, 220, 1047

- Davidson, K. & Ostriker, J. P. 1973, *ApJ*, 179, 585  
 Ducci, L., Sidoli, L., Mereghetti, S., Paizis, A., & Romano, P. 2009, *MNRAS*, in press, arXiv:0906.3185  
 Giunta, A., Bozzo, E., Bernardini, F., et al. 2009, *MNRAS*, in press, arXiv:0905.4866  
 Lefever, K., Puls, J., & Aerts, C. 2007, *A&A*, 463, 1093  
 Levine, A. M. & Corbet, R. 2006, *Astron. Tel.*, 940  
 Negueruela, I., Smith, D. M., Reig, P., Chaty, S., & Torrejón, J. M. 2006, in *Proceedings of the “The X-ray Universe 2005”*, 26-30 September 2005, El Escorial, Madrid, Spain. Ed. by A. Wilson. ESA SP-604, Volume 1, 165  
 Poole, T. S., Breeveld, A. A., & Page, M. J., et al., 2008, *MNRAS*, 383, 627  
 Rahoui, F. & Chaty, S. 2008, *A&A*, 492, 163  
 Rappaport, S. A. & Joss, P. C. 1983, in *Accretion-Driven Stellar X-ray Sources*, ed. W. H. G. Lewin & E. P. J. van den Heuvel, 1–39  
 Romano, P., Sidoli, L., Cusumano, G., et al. 2009a, *MNRAS*, in press, arXiv:0907.1289  
 Romano P., Sidoli L., Cusumano G., Vercellone S., Mangano V., Krimm H. A., 2009b, *ApJ*, 696, 2068  
 Roming, P. W. A., Kennedy, T. E., & Mason, K. O., et al., 2005, *Space Science Reviews*, 120, 95  
 Searle, S. C., Prinja, R. K., Massa, D., & Ryans, R. 2008, *A&A*, 481, 777  
 Sguera, V., Barlow, E. J., Bird, A. J., et al. 2005, *A&A*, 444, 221  
 Sguera, V., Bazzano, A., Bird, A. J., et al. 2006, *ApJ*, 646, 452  
 Sguera, V., Hill, A. B., Bird, A. J., et al. 2007, *A&A*, 467, 249  
 Shimada M. R., Ito M., Hirata B., Horaguchi T., 1994, in Balona L. A., Henrichs H. F., Le Contel J. M., eds, *Pulsation; Rotation; and Mass Loss in Early-Type Stars Vol. 162 of IAU Symposium, Radiatively driven winds of OB stars*, 487  
 Skinner, G., Tueller, J., Beckmann, V., Corbet, R., Farrell, S., Krimm, H.A., Markwardt, C., 2008, in *proceedings of 7th INTEGRAL Workshop, PoS(Integral08)130*  
 Sidoli, L. 2009, *Advances in Space Research*, 43, 1464  
 Sidoli, L., Paizis, A., & Mereghetti, S. 2006, *A&A*, 450, L9  
 Sidoli L., Romano P., Mangano V., et al., 2008, *ApJ*, 687, 1230  
 Swank, J. H., Smith, D. M., & Markwardt, C. B. 2007, *Astron. Tel.*, 999

This paper has been typeset from a  $\text{\LaTeX}$  file prepared by the author.

[t]

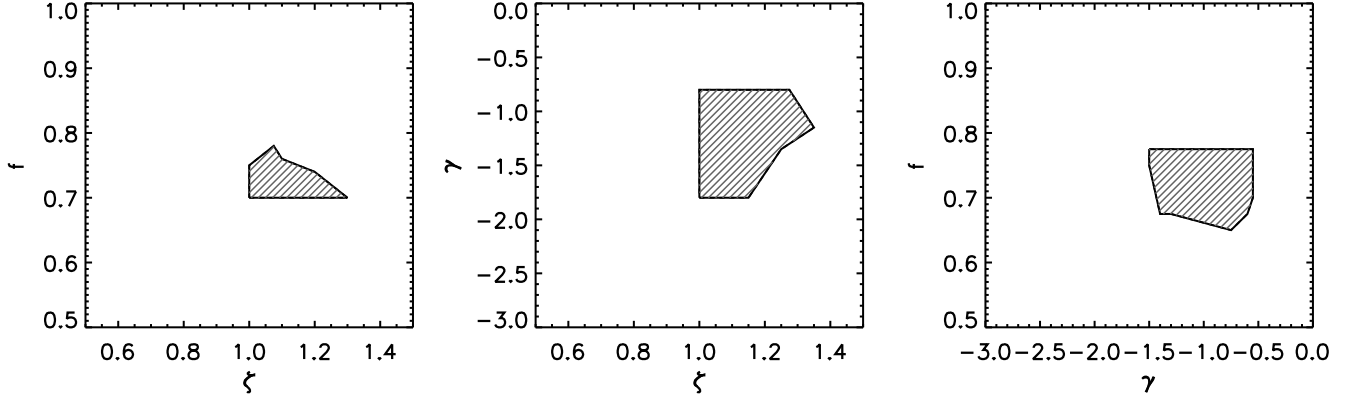


**Figure 7.** Graphs of the allowed parameters  $\zeta$ ,  $f$ ,  $\gamma$  (filled region), obtained from the comparison between the observed and the calculated light curves.